

Robust optical mode converter based on topological waveguide arrays

Yu-Xiang Xu(徐宇翔), Wen-Jian Tang(唐文剑), Li-Wei Jiang(姜力炜), De-Xing Wu(吴德兴), Heng Wang(王恒), Bing-Cong Xu(许冰聪), Lin Chen(陈林)

Citation: Chin. Phys. B, 2024, 33 (**6**): 060306. DOI: 10.1088/1674-1056/ad3811
Journal homepage: http://cpb.iphy.ac.cn; http://iopscience.iop.org/cpb

What follows is a list of articles you may be interested in

Quantum circuit-based proxy blind signatures: A novel approach and experimental evaluation on the IBM quantum cloud platform

Xiaoping Lou(娄小平), Huiru Zan(咎慧茹), and Xuejiao Xu(徐雪娇)
Chin. Phys. B, 2024, 33 (**5**): 050307. DOI: 10.1088/1674-1056/ad22d5

Quantum generative adversarial networks based on a readout error mitigation method with fault tolerant mechanism

Run-Sheng Zhao(赵润盛), Hong-Yang Ma(马鸿洋), Tao Cheng(程涛), Shuang Wang(王爽), and Xing-Kui Fan(范兴奎)
Chin. Phys. B, 2024, 33 (**4**): 040304. DOI: 10.1088/1674-1056/ad02e7

Progress and realization platforms of dynamic topological photonics

Qiu-Chen Yan(闫秋辰), Rui Ma(马睿), Xiao-Yong Hu(胡小永), and Qi-Huang Gong(龚旗煌)
Chin. Phys. B, 2024, 33 (**1**): 010301. DOI: 10.1088/1674-1056/acf284

Anomalous non-Hermitian dynamical phenomenon on the quantum circuit

Chenxiao Dong(董陈潇), Zhesen Yang(杨哲森), Jinfeng Zeng(曾进峰), and Jiangping Hu(胡江平)
Chin. Phys. B, 2023, 32 (**7**): 070305. DOI: 10.1088/1674-1056/acce9a

Efficient and stable wireless power transfer based on the non-Hermitian physics

Chao Zeng(曾超), Zhiwei Guo(郭志伟), Kejia Zhu(祝可嘉), Caifu Fan(范才富), Guo Li(李果), Jun Jiang(江俊), Yunhui Li(李云辉), Haitao Jiang(江海涛), Yaping Yang(羊亚平), Yong Sun(孙勇), and Hong Chen(陈鸿)
Chin. Phys. B, 2022, 31 (**1**): 010307. DOI: 10.1088/1674-1056/ac3815

Robust optical mode converter based on topological waveguide arrays

Yu-Xiang Xu(徐宇翔)[†], Wen-Jian Tang(唐文剑)[†], Li-Wei Jiang(姜力炜), De-Xing Wu(吴德兴), Heng Wang(王恒), Bing-Cong Xu(许冰聪), and Lin Chen(陈林)[‡]

Wuhan National Laboratory for Optoelectronics and School of Optical and Electronic Information, Huazhong University of Science and Technology, Wuhan 430074, *China*

(Received 9 January 2024; revised manuscript received 14 March 2024; accepted manuscript online 27 March 2024)

Optical mode converters are essential for enhancing the capacity of optical communication systems. However, fabrication errors restrict the further improvement of conventional mode converters. To address this challenge, we have designed an on-chip TE_0–TE_1 mode converter based on topologically protected waveguide arrays. The simulation results demonstrate that the converter exhibits a mode coupling efficiency of 93.5% near 1550 nm and can tolerate a relative fabrication error of 30%. Our design approach can be extended to enhance the robustness for other integrated photonic devices, beneficial for future development of optical network systems.

Keywords: on-chip integrated photonic devices, topological photonics, mode converter, robustness

PACS: 03.65.Vf, 42.82.Et, 85.60.–q **DOI:** 10.1088/1674-1056/ad3811

1. Introduction

In recent years, on-chip integrated photonic devices have gradually attracted research interest due to their advantages, such as low loss, high integration, and high controllability. On-chip integrated photonic devices represented by on-chip optical waveguides,[1] couplers,[2–4] splitters,[5] resonators,[6] mode converter,[7–10] gratings,[11] lasers,[11,13] optical modulators,[14,15] and photo-detectors[16] have matured in terms of design principles and manufacturing processes over decades. However, current integrated photonic devices are constrained by design principles, intrinsic material properties, and fabrication errors. For example, the sensitivity of directional couplers to gap distances,[17] material dispersion effects,[18] and errors in splicing and etching during fabrication can degrade device performance,[19] leading to functional failure for practical applications. In addition, the mainstream fabrication processes, including photolithography and electron beam lithography (EBL), are limited by the diffraction-limit resolution,[20] making it difficult to further improve fabrication accuracy. Moreover, micro/nano fabrication inevitably results in local defects on the device surface or interior,[21] which also limits the integration level of photonic chips, thereby constraining further performance improvement. Controlling the adverse effects of the aforementioned limiting factors has been challenging in the development of integrated photonics.

On-chip integrated photonic devices based on the principles of topological photonics have been widely studied due to their robustness to fabrication errors. Topological photonics is an interdisciplinary field that applies principles of topology to the field of optics.[22–26] In recent years, research in topological photonics has revealed many unique physical phenomena not previously observed in traditional optical systems. These include phenomena such as one-way transport of photonic topological edge states (TESs),[27] deformation-insensitive localized resonance effects,[28] and edge-to-edge topological light transport.[29] These findings provide valuable insights for overcoming the bottleneck issues in on-chip optical isolators,[30] high-performance on-chip lasers,[31] on-chip optical quantum computing units,[32,33] and other devices. In particular, researches on photonic TESs have shown their extremely high tolerance to structural errors, emerging as a hot topic in the field of topological photonics. Currently, there have been a great deal of development in robust on-chip directional couplers/splitters,[34] fishbone waveguides,[35] and optical resonant cavities[36] based on photonic TESs. The development of on-chip integrated photonic devices that support photonic TESs holds the promise for overcoming performance bottlenecks caused by various limiting factors and even for developing entirely novel functional devices. This has the potential to significantly expand the possibilities for further development of future optical communication and optical network systems.

In this paper, we propose an on-chip silicon-based optical waveguide arrays that support TESs. We have designed an on-chip TE_0–TE_1 mode converter that utilizes the mode coupling between TESs. This converter is capable of tolerating errors that may arise during the EBL fabrication process. Firstly, we have designed on-chip waveguide arrays based on the Su–Schrieffer–Heeger (SSH) model and analyzed the topological phase of the system through calculating the winding number. We have successfully proved the existence of TESs under the non-trivial topological phase. Subsequently, we have designed directional couplers between two boundary waveguides based on the coupling between two TESs. Additionally, we found that using waveguides of specific widths can achieve mode conversion between TE_0 and TE_1 modes between the

[†]These authors contributed equally to this work.

[‡]Corresponding author. E-mail: chen.lin@mail.hust.edu.cn

© 2024 Chinese Physical Society and IOP Publishing Ltd

two boundary waveguides of the arrays. This process is robust to the errors of the waveguide gap distances. We have conducted finite-difference time-domain (FDTD) simulations, which show that the converter exhibits a coupling efficiency of 93.5% near 1550 nm and can withstand up to 30% relative EBL fabrication errors.

2. Theoretical analysis

2.1. Topologically protected on-chip silicon-based waveguide arrays

Firstly, we have constructed on-chip silicon waveguide arrays with height $h = 220$ nm on a 2-μm silica substructure with an infinite number of unit-cells based on the SSH model, as shown in Fig. 1(a). The working wavelength of the waveguide arrays is 1550 nm. Here, $w_1 = w_2 = 400$ nm are the widths of the two silicon waveguides in a unit-cell, which are related to the propagation coefficients k_1 and k_2 of the fundamental modes in an individual waveguide. Additionally, $g_{12} = 220$ nm and $g_{21} = 185$ nm are the inter-cell and intra-cell gap distances between the two waveguides, respectively, which govern the hopping strength in the SSH model, *i.e.*, the coupling coefficients c_{12} and c_{21} between the waveguides [Fig. 1(a)]. We combine the previous research results and use FDTD simulation to calculate the variation of the fundamental mode propagation coefficient, k, with the waveguide width w[30]

$$k = k_0 + \alpha_1 w + \alpha_2 w^2. \tag{1}$$

Here, $k_0 = 3.61\ \mu\text{m}^{-1}$, $\alpha_1 = 17.1\ \mu\text{m}^{-2}$, and $\alpha_2 = -10.3\ \mu\text{m}^{-3}$. It should be noted that equation (1) is applicable to the waveguide width ranging from 300 nm to 900 nm. Consequently, we can obtain the propagation constants of the fundamental mode in the waveguide, $k_1 = k_2 = 8.8292\ \mu\text{m}^{-1}$. As far as we know, the coupling coefficients between the waveguides generally follow the relationship as

$$c = c_0 \mathrm{e}^{-\beta g}, \tag{2}$$

where g is the gap distance between two waveguides, β and c_0 are undetermined coefficients that are determined by the material of waveguides, the width of waveguides and working wavelength.[37] We have conducted FDTD simulation to study the coupling process of light between the two waveguides under the two gap distances g, associated with two coupling coefficients c. Here, the gap distance g is an arbitrary width ranging from 100 nm to 300 nm. The coupling distance L_c is referred to as the minimum distance as the optical field is completely transported from one waveguide to another. The corresponding coupling coefficient c can then be retrieved by $c = \pi/(2L_c)$. By incorporating the two groups of c and g into Eq. (2), we are able to determine c_0 and β, with $c_0 = 0.874\ \mu\text{m}^{-1}$ and $\beta = 5.42\ \mu\text{m}^{-1}$. Afterwards, by incorporating the initial waveguide gap distances $g_{12} = 220$ nm and $g_{21} = 185$ nm into Eq. (2), we can obtain the coupling coefficients as $c_{12} = 0.265\ \mu\text{m}^{-1}$ and $c_{21} = 0.321\ \mu\text{m}^{-1}$.

The real-space Hamiltonian can be expressed as[38]

$$\boldsymbol{H} = \begin{bmatrix} k & c_{12} & & & & & \\ c_{12} & k & c_{21} & & & & \\ & c_{21} & k & c_{12} & & & \\ & & c_{12} & k & c_{21} & & \\ & & & c_{21} & k & c_{12} & \\ & & & & c_{12} & k & \end{bmatrix}. \tag{3}$$

It is worth noting that, the waveguide arrays we have set are of infinite size, which means that the dimension of the Hamiltonian tends to infinity. Notably, this does not facilitate the computation and analysis of eigenvalues and eigenvectors. Therefore, we have transformed it into the Hamiltonian in momentum space through Fourier transformation[38]

$$\boldsymbol{H}(k) = \begin{bmatrix} k & c_{12} + c_{21}\mathrm{e}^{-\mathrm{i}k_x} \\ c_{12} + c_{21}\mathrm{e}^{\mathrm{i}k_x} & k \end{bmatrix}, \tag{4}$$

where k_x is the wave vector in the first Brillouin zone. The Hamiltonian in momentum space can be further expressed as a linear combination of Pauli matrices $(\sigma_0, \sigma_x, \sigma_y, \sigma_z)$:

$$\boldsymbol{H}(k) = k\sigma_0 + (c_{12} + c_{21}\cos k_x)\,\sigma_x + c_{21}\sin k_x \sigma_y. \tag{5}$$

It can be observed that the coefficients $(c_{12} + c_{21}\cos k_x)$ and $c_{21}\sin k_x$ form a circle in the parameter space $\sigma_x O \sigma_y$ with a center at $(c_{12}, 0)$ and a radius of c_{21}. As the parameter k_x sweeps through the interval $[0, 2\pi]$, the vector $(c_{12} + c_{21}\cos k_x, c_{21}\sin k_x)$ will trace out a circular trajectory as described above. Based on the definition of the winding number

$$V = \frac{1}{2\pi\mathrm{i}} \int_{-\pi}^{\pi} \frac{\partial \log(c_{12} + c_{21}\mathrm{e}^{-\mathrm{i}k_x})}{\partial k_x} \mathrm{d}k_x$$

in one-dimensional SSH model,[38] the circle does not enclose the origin point when $c_{12} > c_{21}$, resulting in $V = 0$, indicating that the system is in a topologically trivial phase [blue circle in Fig. 1(b). Conversely, when $c_{12} < c_{21}$, the circle encloses the origin point, leading to $V = 1$, suggesting that the system is topologically protected [red circle in Fig. 1(b)]. Therefore, under open boundary conditions, our model support two TESs, which is determined by the bulk–edge correspondence.[38]

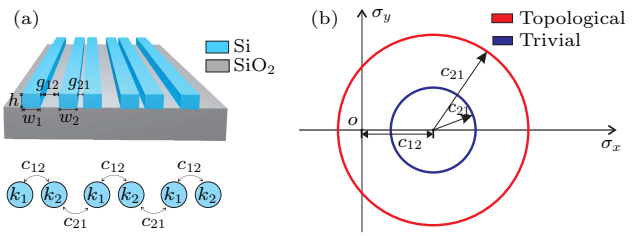


Fig. 1. Optical silicon waveguide arrays with topological protection. (a) The geometry model and tight-binding model of the waveguide arrays, where w_1 and w_2 represent the waveguide widths governing the waveguide propagation constants k_1 and k_2, respectively, g_{12} and g_{21} are the gap sizes between waveguides, determining coupling coefficient c_{12} and c_{21}, respectively. (b) The winding number of the waveguide arrays with different c_{12} and c_{21}.

2.2. Topological edge states

The theoretical analysis in Subsection 2.1 has predicted the existence of TESs in the topological waveguide arrays with finite number of unit-cells. Next, we will use an on-chip waveguide arrays with 3 unit-cells to verify the existence of TESs. Because our waveguide arrays consist of 6 waveguides, we have used a 6×6 Hamiltonian to characterize the tight-binding model of our system. The system therefore supports 6 eigenmodes. According to bulk–boundary correspondence, the TESs always appear in the middle of the energy band (eigen-spectrum). As a result, the TESs are the 3rd and 4th eigenmodes. Through mode analysis using FDTD simulation, we have successfully observed the TESs localized at the edge of the waveguide arrays. As shown in [Figs. 2(a) and 2(b)], the 3rd and 4th eigenmodes of the waveguide arrays are TESs. It is worth noting that, mode 3 and mode 4 exhibit opposite phase distributions [Figs. 2(c) and 2(d)].

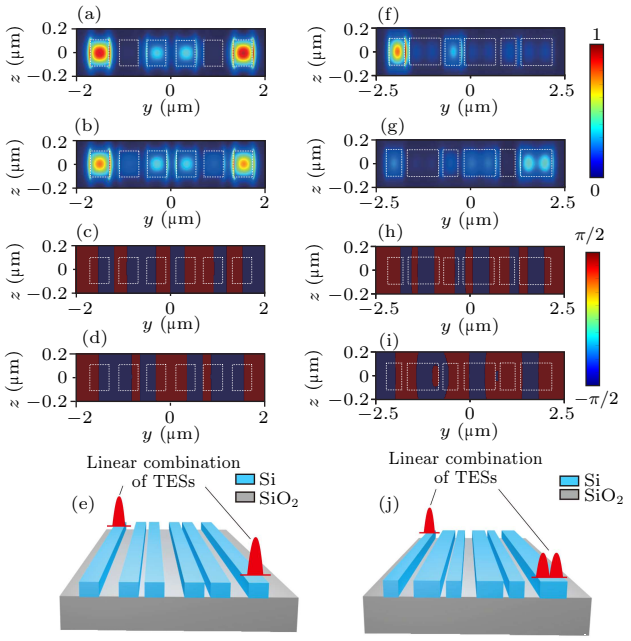


Fig. 2. The coupling effect between TESs. (a)–(b) The field intensity distribution of TES1 and TES2, $|E|^2$, in the waveguide arrays in Subsection 2.3. (c)–(d) The phase distribution of TES1 and TES2 in the waveguide arrays in Subsection 2.3. (e) The directional coupling between the two TESs in the waveguide arrays in Subsection 2.3. (f)–(g) The intensity distribution of TES1 and TES2, $|E|^2$, in the waveguide arrays in Subsection 2.4. (h)–(i) The phase distribution of TES1 and TES2 in waveguide arrays in Subsection 2.4. (j) The mode converting between the two TESs in the waveguide arrays in Subsection 2.4.

2.3. Coupling between topological edge states

Based on the mode analysis results obtained in Subsection 2.2, it can be observed that, the spatial distribution of the field intensity $|E|^2$ of the two TESs are symmetric [Figs. 2(a) and 2(b)]. This is because, the finite size effect weakens the topological protection, resulting in band degeneracy breaking and the coupling between the TESs.[39] Considering the opposite phase distributions between the two TESs [Figs. 2(c) and 2(d)], the coupling between TESs will result in directional coupling between the two edge waveguides. As shown in Fig. 2(e), when the light is localized at the left boundary of the waveguide arrays, it can be approximately regarded as the direct superposition of two TESs, i.e., TES1 + TES2. Since the mode propagation constants of the two TESs are non-degenerate, an optical path difference, $\Delta\beta = (\beta_{\mathrm{TES1}} - \beta_{\mathrm{TES2}})L_{\mathrm{c}}$, will arise between the two TESs after the two TESs propagate over a distance L_{c}. When $\Delta\beta = \pi$, i.e., $L_{\mathrm{c}} = 37.16$ μm, the linear superposition of the two TESs is transformed into the form of TES1–TES2, rendering the light localization is transferred from the left boundary to the right boundary, thereby achieving directional coupling between the TESs.[34] It is worth noticing that, the eigenvalues of the two TESs are degenerate when the number of the unit-cell in our structure is quite large, i.e., approximately infinite. As a result, the coupling length L_{c} becomes infinite because the value of $\beta_{\mathrm{TES1}} - \beta_{\mathrm{TES2}}$ is zero. Thus, the two TESs are uncoupled.

2.4. $\mathrm{TE_0}$–$\mathrm{TE_1}$ mode converter based on topological edge states

Based on the aforementioned theoretical foundation, we have designed a topological mode converter that can convert the fundamental mode $\mathrm{TE_0}$ into the higher-order mode $\mathrm{TE_1}$. Since the higher-order mode $\mathrm{TE_1}$ in the waveguide has a smaller effective refractive index than the fundamental mode $\mathrm{TE_0}$, the fundamental mode $\mathrm{TE_0}$ in the narrow waveguide and the higher-order mode $\mathrm{TE_1}$ in the wide waveguide can share the same effective refractive index through the judicious control of waveguide widths. We found that when the waveguide widths in Fig. 1(a) are $w_1 = 400$ nm and $w_2 = 830$ nm, the aforementioned condition can be satisfied. We then set the intra-cell waveguide gap distances $g_{12} = 140$ nm and the inter-cell waveguide gap distances $g_{21} = 120$ nm [Fig. 1(a)], the waveguide arrays will be topologically protected, according to the analysis discussed in Subsection 2.1. Consequently, it can support two TESs with opposite phase distributions. Using the method described in Subsection 2.1, we have retrieved the variables in the corresponding real-space Hamiltonian for the waveguide arrays: $c_0 = 0.959\ \mu\mathrm{m}^{-1}$, $\beta = 11.3\ \mu\mathrm{m}^{-1}$, $c_{12} = 0.197\ \mu\mathrm{m}^{-1}$, and $c_{21} = 0.247\ \mu\mathrm{m}^{-1}$. Through modeling and simulation analysis by FDTD simulation, we have successfully observed the two TESs by analyzing the field intensity and phase distribution of each eigenmode electric field [Figs. 2(f)–2(i)]. It is worth noticing that the field intensity distributions of TESs are asymmetric because the coupling strengths between the waveguides in topological mode converter are weaker than those in topological directional coupler.[38,39]

As described in Subsection 2.3, the optical field that is localized at a single boundary of the waveguide arrays can be regarded as a linear superposition of the two TESs. However, unlike the design of the topological directional coupler mentioned in Subsection 2.3, the waveguides in the current waveguide arrays with larger widths support the $\mathrm{TE_1}$ mode. Therefore, the proposed waveguide arrays can not only couple light from one boundary to another, but also achieve the conversion

between the TE_0 and TE_1 modes [Fig. 2(j)]. Using the principle of directional coupling, we have calculated the coupling length L_m of the topological mode converter, $L_m = 27.25$ μm.

3. Simulated demonstration

We use FDTD simulation to conduct a series of modeling and simulation to validate the performance of light propagation in the topological directional couplers and topological mode converters, and to verify the robustness of topologically protected devices.

3.1. Ordinary directional couplers and topological directional couplers

Based on the geometrical parameters provided in Subsection 2.1, we have studied the ordinary directional couplers and topological directional couplers on a silica substrate.

We set a mode source having the mode distributions of TE_0 mode at the input port of the devices, labeled by the red arrows in Fig. 3. We have simulated the transmission optical fields of the ordinary directional couplers and topological directional couplers. Figure 3(a) illustrates the transmission of light in the ordinary directional coupler. To quantitatively evaluate the directional coupling performance of the device, we have defined the coupling efficiency

$$\tau = \frac{|E_o|^2}{|E_i|^2} \times 100\%$$

as the ratio of the desired mode to the input mode, where $|E_i|^2$ is the input light intensity and $|E_o|^2$ is the light intensity of the desired mode. Both $|E_i|^2$ and $|E_o|^2$ can be extracted from the detector set in the FDTD simulation. The coupling efficiency τ of the ordinary directional coupler as designed is 98.7%. Next, we have evaluated the robustness of the topological directional coupler by modifying the waveguide gap distances. We define the relative error of the waveguide gap distances as $\varepsilon = \Delta g/g$. We have added relative errors of $\varepsilon = 10\%$ [Fig. 3(b)] and $\varepsilon = 20\%$ [Fig. 3(c)] to the ordinary directional coupler and have simulated the optical field propagation. The coupling efficiency τ of the ordinary directional coupler suffers a significant decay from $\tau = 98.7\%$ [Fig. 3(a)] to $\tau = 83.5\%$ [Fig. 3(b)] and $\tau = 57.9\%$ [Fig. 3(c)].

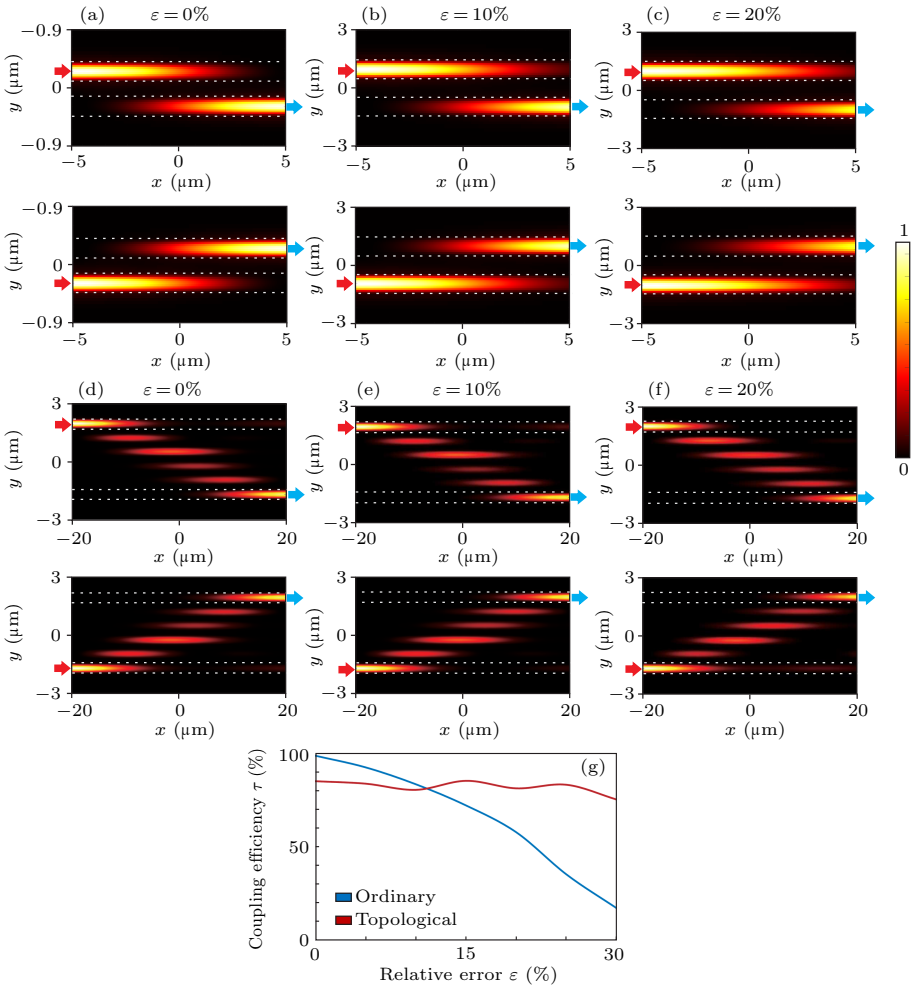


Fig. 3. Simulation on light propagation in ordinary directional coupler and the topological directional coupler. The red and blue arrows label the input and out ports of the device, respectively. (a) The ordinary directional coupler without relative errors. (b)–(d) The topological directional couplers with relative errors $\varepsilon = 0\%$ (b), $\varepsilon = 10\%$ (c), and $\varepsilon = 20\%$ (d). The upper panels of these figures show the directional couplings from upper boundary to lower boundary of waveguide arrays, while the lower panels refer to the opposite processes. (g) The coupling efficiency τ of ordinary (the blue line) and topological (the red line) directional couplers as a function of different relative errors ε.

We have also simulated the propagation of light in the topological directional coupler based on the same geometry parameters. As shown in Fig. 3(d), under the condition of no relative error, the coupling efficiency τ of the topological directional coupler reaches $\tau = 85.2\%$. We have added relative errors of $\varepsilon = 10\%$ [Fig. 3(e)] and $\varepsilon = 20\%$ [Fig. 3(f)] to the topological directional coupler and simulates the optical field propagation as well. The coupling efficiency τ of the topological directional coupler remains at $\tau = 80.6\%$ and $\tau = 81.4\%$. In order to exhibit the robustness of topological directional coupler, we have stimulated more groups of ordinary and topological directional coupler with relative errors ε ranging from 0% to 30% and calculated the coupling efficiency τ. The effect of relative error ε on the coupling efficiency τ of ordinary and topological directional coupler is shown in Fig. 3(g). When the relative error is gradually increasing, the coupling efficiency τ of ordinary directional coupler decreases rapidly. When the relative error is $\varepsilon = 0\%$ the coupling efficiency $\tau = 95.1\%$. While the relative error is $\varepsilon = 30\%$, the coupling efficiency is reduced significantly to be $\tau = 35.7\%$, while the topological coupler is kept at a high level of coupling efficiency. In summary, the topological design can significantly improve the robustness of the directional coupler, while maintaining high coupling efficiency.

3.2. Ordinary mode converter and topological mode converter

The ordinary and topological mode converter uses the same geometrical parameters in Subsection 2.4. We also set a mode source at the input port of the devices [labeled by the red arrows in Fig. 4]. The mode source we choose is TE_0 and TE_1 mode, associated with waveguide width $w_1 = 400$ nm and $w_2 = 830$ nm, respectively. We have simulated the transmission optical fields of the ordinary mode converter and topological mode converter.

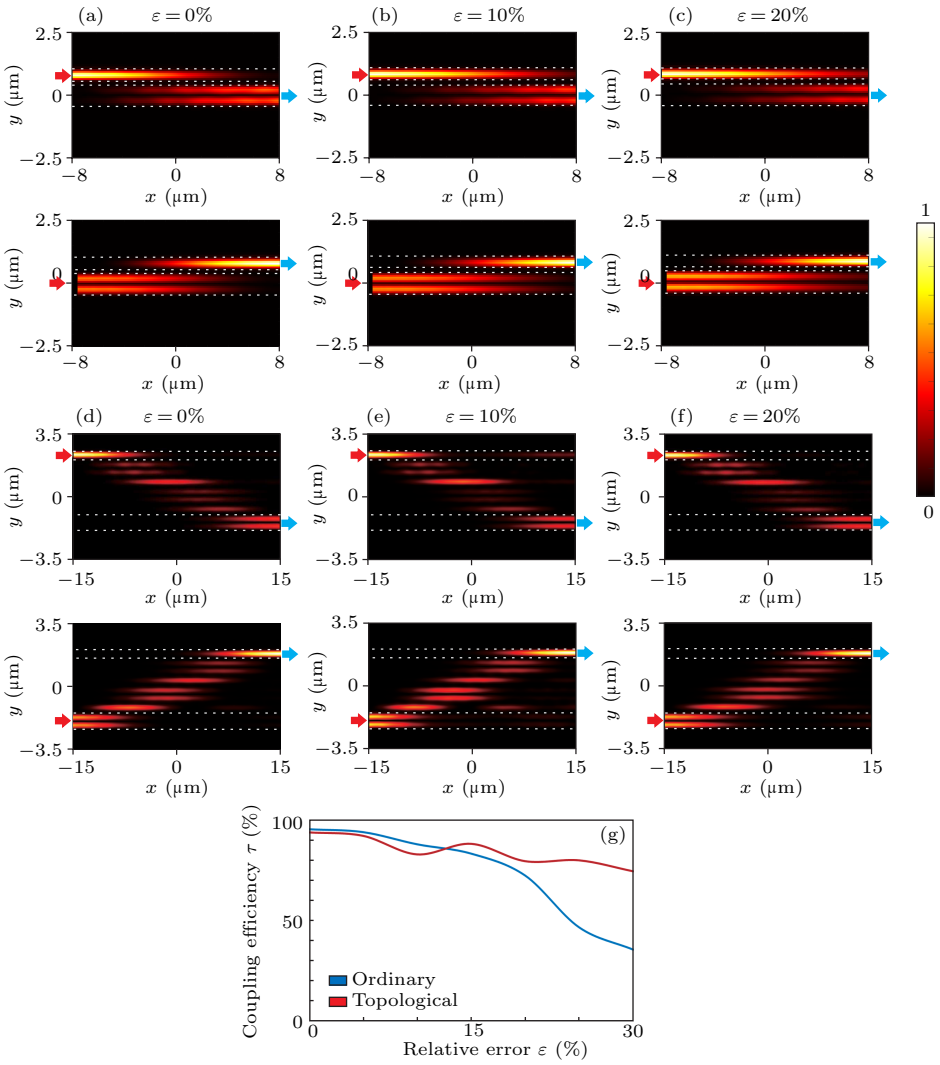


Fig. 4. Simulation on light propagation in ordinary mode converter and the topological mode converter. The red and blue arrows label the input and out ports of the device, respectively. Panels (a)–(c) correspond to the ordinary mode converter with relative errors $\varepsilon = 0\%$ (a), $\varepsilon = 10\%$ (b), and $\varepsilon = 20\%$ (c). Panels (d)–(f) refer to the topological mode converter with relative errors $\varepsilon = 0\%$ (d), $\varepsilon = 10\%$ (e), and $\varepsilon = 20\%$ (f). The upper panels of these figures exhibit the mode conversions from TE_0 to TE_1. The lower panels of these figures show the mode conversions from TE_1 to TE_0. (g) The coupling efficiency τ of ordinary (the blue line) and topological (the red line) mode converters as a function of different relative errors ε.

Figure 4(a) shows the simulation result of the ordinary optical mode converter without the relative error, associated with the coupling efficiency $\tau = 95.1\%$. The coupling efficiency τ reduces sharply, when the relative error is added. When the relative error reaches to the value of $\varepsilon = 10\%$, the coupling efficiency τ of the ordinary mode converter drops to $\tau = 87.7\%$ [as shown in Fig. 4(b)]. When the relative error is $\varepsilon = 20\%$, the coupling efficiency has changed significantly to the value of $\tau = 72.3\%$.

Next, we have performed simulations on the topological optical mode converter. The results are shown in Figs. 4(d)–4(f). The simulation results show that the coupling efficiency of the entire topological mode converter under the error-free condition is $\tau = 93.5\%$ [as shown in Fig. 4(d)]. When the relative errors ε are 10% [shown in Fig. 4(e)], and 20% [shown in Fig. 4(f)], respectively, the coupling efficiency of the topological mode converter is $\tau = 82.7\%$ and $\tau = 79.4\%$. We have also analyzed the effect of the relative error ε on the coupling efficiency τ of the ordinary and topological mode converters in Fig. 4(g). It is obvious that the coupling efficiency of the ordinary mode converter decays faster than the topological mode converter when the relative error increases. The simulation results have proven that the topological mode converter obtains obviously higher tolerance to relative errors, as opposed to the ordinary mode converter.

4. Conclusion

We have validated the existence of TESs in the SSH model using on-chip silicon waveguide arrays, and have numerically demonstrated on-chip directional couplers and mode converters based on the coupling between TESs. Through unique topological protection design, the topological directional coupler and mode converter can tolerate a certain degree of fabrication errors, while achieving high-efficiency operation, as has been verified in numerical simulations. We can also design the mode convertor that is capable of transforming TE_0 mode to higher order mode through employing higher or wider waveguides. By extending our design approach to other on-chip functional devices, we can potentially realize a series of robust on-chip functional devices, such as splitters, adiabatic couplers, and multiplexers/demultiplexers. From the perspective of practical application, these topologically protected basic units can be used to construct on-chip optical systems with top-level functionality, such as optical interconnect networks, optical routing networks, and optical information processors. This can reduce the overall dependence of these systems on fabrication accuracy, potentially lowering the difficulty of fabricating on-chip integrated photonics devices and providing a novel approach for designing low-cost, highly integrated on-chip optical systems.

Acknowledgements

Project supported by the National Undergraduate Training Projects for Innovation and Entrepreneurship (Grant No. 5003182007), the National Natural Science Foundation of China (Grant No. 12074137), the National Key Research and Development Project of China (Grant No. 2021YFB2801903), and the Natural Science Foundation from the Science, Technology, and Innovation Commission of Shenzhen Municipality (Grant No. JCYJ20220530161010023).

References

[1] Blanco-Redondo A, Andonegui I, Collins M J, Harari G, Lumer Y, Rechtsman M C, Eggleton B J and Segev M 2016 *Phys. Rev. Lett.* **116** 163901
[2] Ding Y, Xu J, Da Ros F, Huang B, Ou H and Peucheret C 2013 *Opt. Express* **21** 10376
[3] Li A D, Dong J J, Wang J, Cheng Z W, Ho J S, Zhang D W, Wen J, Zhang X L, Chan C T, Andrea Alù, Qiu C W and Chen L 2020 *Phys. Rev. Lett.* **125** 187403
[4] Meng Y, Wu X X, Shen Y X, Liu D, Liang Z X, Zhang X and Jensen Li 2022 *Sci. China-Phys. Mech. Astron.* **65** 224611
[5] Hu Y, Yu M, Zhu D, Sinclair N, Shams-Ansari A, Shao L, Holzgrafe J, Puma E, Zhang M and Lončar M 2021 *Nature* **599** 587
[6] Wan X, Peng C Y, Li G, Yang J H and Qi X Y 2023 *Chin. Phys. B* **32** 114208
[7] Shu X Q, Li A D, Hu G W, Wang J, Alù A and Chen L 2022 *Nat. Commun.* **13** 2123
[8] Li A D, Chen W J, Wei H, Lu G W, Alù A, Qiu C W and Chen L 2022 *Phys. Rev. Lett.* **129** 127401
[9] Li A D, Wei H, Michele Cotrufo, Chen W J, Sander Mann, Ni X, Xu B C, Chen J F, Wang J, Fan S H, Qiu C W, Alù A and Chen L 2023 *Nat. Nanotechnol.* **18** 706
[10] Shu X Q, Zhong Q, Hong K, You O B, Wang J, Hu G W, Alù A, Zhang S, Demetrios N Christodoulides and Chen L 2024 *Light. Sci. Appl.* **13** 65
[11] Wang J, Ashrafi R, Adams R, Glesk I, Gasulla I, Capmany J and Chen L R 2016 *Sci. Rep.* **6** 30235
[12] Zhou Z, Yin B and Michel J 2015 *Light Sci. Appl.* **4** e358
[13] Liang Y, Li C, Huang Y Z and Zhang Q 2020 *ACS Nano* **14** 14375
[14] Amin R, Suer C, Ma Z, Sarpkaya I, Khurgin J B, Agarwal R and Sorger V J 2017 *Solid State Electron.* **136** 101
[15] Wang C, Zhang M, Chen X, Bertrand M, Shams-Ansari A, Chandrasekhar S, Winzer P and Lončar M 2018 *Nature* **562** 101
[16] Assefa S, Xia F and Vlasov Y A 2010 *Nature* **464** 80
[17] Marcatili E A 1969 *Bell Syst. Tech. J.* **48** 2071
[18] Cooper M L, Gupta G, Schneider M A, Green W M, Assefa S, Xia F, Gifford D K and Mookherjea S 2010 *Opt. Lett.* **35** 3030
[19] Groves T R 2014 *Nanolithography* (Sawston Cambridge: Woodhead Publishing) pp. 80–115
[20] Awad M and Cheville R A 2005 *Appl. Phys. Lett.* **86** 221107
[21] Rajurkar K P, Levy G, Malshe A, Sundaram M, McGeough J, Hu X, Resnick R, DeSilva A and DeSilva A 2006 *CIRP Ann. Manuf. Technol.* **55** 643
[22] Chen J F and Li Z Y 2022 *Chin. Phys. B* **31** 114207
[23] Xu Z H, Xia X and Chen S 2022 *Sci. China-Phys. Mech. Astron.* **65** 227211
[24] Xu H S and Jin L 2023 *Phys. Rev. Res.* **5** L042005
[25] Wu H C, Xu H S, Xie L C and Jin L 2024 *Phys. Rev. Lett.* **132** 083801
[26] Wang P, Jin L and Song Z 2024 *Phys. Rev. B* **109** 115406
[27] Lustig E, Weimann S, Plotnik Y, Lumer Y, Bandres M A, Szameit A and Segev M 2019 *Nature* **567** 356
[28] Zhu X Y, Fu J C, Ding F, Jin Y and Wu A M 2018 *Sci. Rep.* **8** 15240

[29] Xiao L, Zhan X, Bian Z H, Wang K, Zhang X, Wang X P, Li J, Mochizuki K, Kim D, Kawakami N, Yi W, Obuse H, Sanders B C and Xue P 2017 *Nat. Phys.* **13** 1117

[30] Krauss T F 2008 *Nat. Photon.* **2** 448

[31] Dokania R K and Apsel A B 2009 *Proceedings of the 19th ACM Great Lakes Symposium on VLSI*, May 10–12, 2009, Boston, USA, p. 275

[32] Thompson M G, Politi A, Matthews J C and O'Brien J L 2011 *IET Circuits Dev. Syst.* **5** 94

[33] Chen Y, He X T, Cheng Y J, Qiu H Y, Feng L T, Zhang M, Dai D X, Guo G C, Dong J W and Ren X F 2021 *Phys. Rev. Lett.* **126** 230503

[34] Song W, Sun W, Chen C, Song Q, Xiao S, Zhu S and T Li 2020 *Laser Photon. Rev.* **14** 1900193

[35] Zhao X J, Hamed Dalir, Xu X C and Chen R T 2017 *Appl. Phys. Express* **10** 072502

[36] Reithmaier J P, Sęk G, Löffler A, Hofmann C, Kuhn S, Reitzenstein S, Kulakovskii V D, Reinecke T L and Forchel A 2004 *Nature* **432** 197

[37] Chuang S L 1987 *J. Light. Technol.* **5** 5

[38] Asbóth J K, Oroszlány L and Pályi A 2016 *A Short Course on Topological Insulators*, Vol. 919 (Switzerland: Springer International Publishing) pp. 1–22

[39] Xu B C, Xie B Y, Xu L H, Deng M, Chen W, Wei H, Dong F, Wang J, Qiu C W, Zhang S and Chen L 2023 *Adv. Photon.* **5** 036005